INTERNATIONAL JOURNAL FOR NUMERICAL METHODS IN FLUIDS
Int. J. Numer. Meth. Fluids 2004; **46**:435–455 (DOI: 10.1002/fld.761)

Free boundary viscous flows at micro and mesolevel during liquid composites moulding process

Zuzana Dimitrovová[1,*,†,‡] and Suresh G. Advani[2,§]

[1]*Department of Mechanical Engineering, IST, Lisbon, Portugal*
[2]*Department of Mechanical Engineering, Associate Director of Center for Composite Materials, University of Delaware, DE, U.S.A.*

SUMMARY

Numerical simulation aspects, related to low Reynolds number free boundary viscous flows at micro and mesolevel during the resin impregnation stage of the liquid composite moulding process (LCM), are presented in this article. A free boundary program (FBP), developed by the authors, is used to track the movement of the resin front accurately by accounting for the surface tension effects at the boundary. Issues related to the global and local mass conservation (GMC and LMC) are identified and discussed. Unsuitable conditions for LMC and consequently GMC are uncovered at low capillary numbers, and hence a strategy for the numerical simulation of such flows is suggested.

FBP encompasses a set of subroutines that are linked to modules in ANSYS. FBP can capture the void formation dynamics based on the analysis developed. We present resin impregnation dynamics in two dimensions. Extension to three dimensions is a subject for further research. Several examples are shown and efficiency of different stabilization techniques are compared. Copyright © 2004 John Wiley & Sons, Ltd.

KEY WORDS: resin transfer moulding; liquid composite moulding; free boundary flows; microlevel analysis; mesolevel analysis; surface tension effects

1. INTRODUCTION

Liquid composite moulding (LCM) is a class of processes in which continuous fibres that provide the reinforcement are placed and held stationary by compacting them in a mould cavity, which is in the shape of the part to be manufactured, and a thermoset resin is injected into the mould to cover the empty spaces between the fibres. These continuous fibre

*Correspondence to: Zuzana Dimitrovová, IDMEC, Instituto Superior Técnico, Av. Rovisco pais, 1, 1049-001 Lisbon, Portugal.
†E-mail: zdimitro@dem.ist.utl.pt
‡Researcher of IDMEC/Invited Auxiliary Professor at ISEL.
§Professor.

Contract/grant sponsor: Fundação para a Ciência e a Tecnologia

Published online 16 August 2004

Received 5 May 2003
Revised 22 January 2004

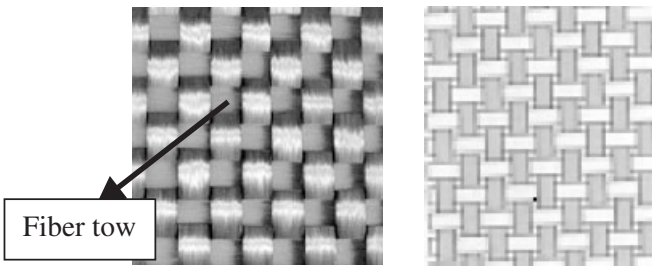

Figure 1. Top view of fibre preform consisting of woven fibre tows (each fibre tow contains 3000 individual fibre filaments). Photograph on the left and a schematic on the right.

reinforcements are called *fibre preforms* and consist of bundles of 2000–5000 fibre filaments, commonly known as *fibre tows*. The fibre tow is usually millimetres in diameter and consists of filaments of about 7–20 μm in diameter. Fibre tows are usually knitted, woven or stitched together as shown in Figure 1.

LCM processes include resin transfer moulding (RTM) and vacuum assisted resin transfer moulding (VARTM), which are the most commonly used methods to manufacture polymer composites. In RTM, the fabrics are cut and placed in a mould, the mould is closed and a thermoset resin of viscosity of the order 100 times that of water is injected through an opening known as an injection port or gate. The goal is to saturate every empty space between the fibre filaments with the resin, before the resin starts to gel and cure. Once the curing process is complete, the composite part is de-moulded (i.e. mould is opened and part is removed). If the resin fails to saturate certain regions of a fibre tow, these regions are called *dry spots* and if the resin partially fills a fibre tow, leaving small regions of the fibre filaments uncovered by resin, they are known as *microvoids*. In principle, no fibre surface should be left uncovered, because dry spots and microvoids serve as sites for initiation of cracks or moisture absorption, which will seriously compromise the properties of the manufactured composite [1].

In most cases, the resin viscosity has a limited 'time window' when its value is low. This is accomplished by adding an inhibitor to the resin. Once the inhibitor is consumed, the curing reaction initiates and the resin molecules crosslink, which substantially increases the viscosity. From the manufacturing viewpoint, one would like the resin to fill the spaces between the fibres before initiating the curing process, because the resin viscosity increases rapidly with degree of cure and high viscosity will slow down or arrest resin flow, creating voids and dry spots. Hence, the understanding of the fluid mechanics and the free surface movement of the resin encompassing the fibre filaments and the fibre tows is crucial to address the issue of avoiding dry spots and microvoids.

The flow of resin into a mould containing fibre preforms can be modelled as flow through porous media. The mould is usually a few millimetres thick and may be a few metres long and wide. Hence, most researchers model this flow on a macroscale with Darcy's law and calculate the average resin velocities to advance the flow in the middle surface of the mould. This 'macroflow' usually requires one to specify average spatial permeability values of the porous media. It does not explicitly take into account the flow around individual fibre filaments or inside a fibre tow. In reality, although 'macroflow' can generally track the overall

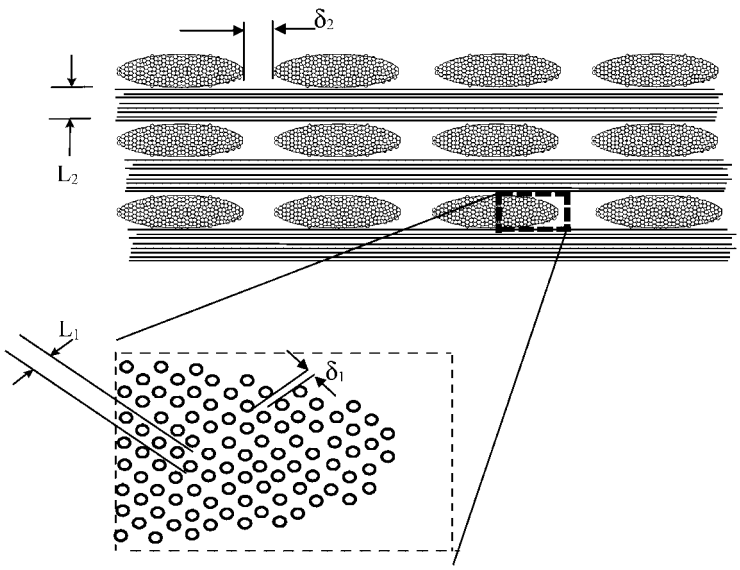

Figure 2. Schematic cross sectional view of fibre preform: $\delta_1 =$ typical pore size of microscopic domain, $L_1 =$ characteristic microscale length; $\delta_2 =$ typical pore size of mesoscopic domain, $L_2 =$ characteristic mesoscale length; $\delta_1 \ll \delta_2,\ L_1 \ll L_2$.

filling of the mould and predict possible unfilled regions, it is incapable of providing details about microvoids and partially filled tows. This difficulty arises because as seen from Figure 2, the fibre preform consists of dual scale pores. The larger pores between the woven fibre tows (*inter-tow* spaces) are of the order of the tow diameter which is usually few millimetres, whereas the pores between every fibre filament within a tow (*intra-tow* spaces) are of the order of the fibre diameter which is few micrometres [2–9]. Therefore, in the terminology of homogenization techniques, except a characteristic dimension of the mould identifying the macroscale, two other characteristic dimensions of different orders can be found, corresponding then to the meso and the microscale (Figure 2). The fluid mechanics on a single fibre strand level is typically called as *microflow*, whereas the flow around a fibre tow is usually described by what is coined as *mesoflow*. To model flow at this scale requires one to address issues of local velocity, specific boundary conditions between the fibre tow surface and the resin, and also introduce the role of surface tension and capillary pressure in the flow physics.

2. MACROFLOW ANALYSIS

Resin impregnation or infiltration is usually modelled as a liquid flowing *slowly* through a porous medium and assumptions of no gravity effects, a sharp flow front and a quasi steady-state process (i.e. steady-state condition is fulfilled at each time step) are generally adopted for the macrolevel filling. Therefore, mass conservation along with Darcy's law are used

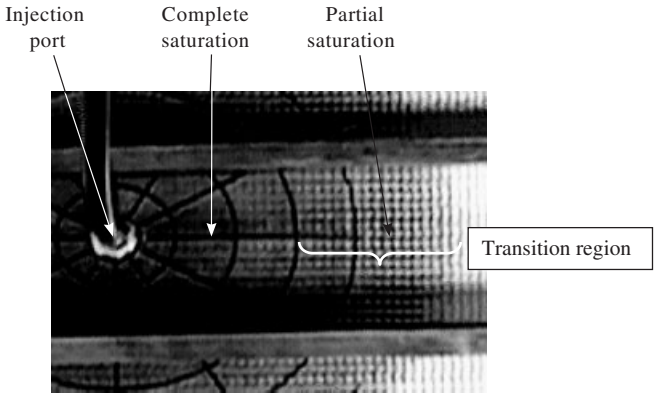

Figure 3. Formation of the transition region in plane of a sample.

as exact homogenization results for macrolevel analysis to formulate the governing equation describing the resin pressure in the saturated section of the mould [10, 11]. The resin flow can be simulated with this physics in large and complex moulds using numerical methods to describe the resin impregnation dynamics. The most common method used is based on finite element/control volume (FE/CV) approach [12, 13]. The mould geometry is discretized with finite elements and a control volume is associated with each element or node. A fill factor is connected with each control volume that indicates the fraction of the control volume filled with the resin. The governing equation is solved only for those elements that have a non-zero fill factor associated with them. The solution is used to update the fill factors, which changes the resin volume in the mould and consequently the domain over which the equation needs to be solved. This procedure is repeated until all the control volumes are filled with resin. The history of the fill factors exemplifies the history of the resin impregnation into the mould. The limitation of this method is that the fill factors in these simulations correspond to a sharp flow front (regions containing the fluid have impregnated all the fibre tows completely and regions ignored by the solution have no resin at all). In reality, because of the dual scale pores, there can be a large region, in which the inter-tow pores are filled, but the fibre tows themselves are not yet completely saturated due to their low permeability; or on the contrary, sometimes fibre tows infiltration can be advanced when compared to the inter-tow spaces, because of the strong capillary action. Both scenarios result in a partially saturated region, formed along the macroscopic flow front or in the neighbourhood of dry spots, known also as a *transition region*, as seen from Figure 3 [2].

In order to capture this partially saturated region, one could model resin advancement by introduction of a new variable, saturation s, which modifies the continuity equation into [14–16]:

$$\phi \frac{\partial s}{\partial t} = -\nabla \cdot \mathbf{v}^{\mathrm{D}}(s) \tag{1}$$

where ϕ is the porosity of the fibre preform defined as $\phi = |V^{\mathrm{p}}|/|V|$, $s = |V^{\mathrm{f}}|/|V^{\mathrm{p}}|$ (V is the representative volume, V^{p} is the pore space of this volume and V^{f} is the part of V^{p} filled by the resin), t is the time, ∇ stands for the spatial gradient and Darcy's velocity $\mathbf{v}^{\mathrm{D}}$ is

the phase averaged velocity defined as $\mathbf{v}^{\mathrm{D}} = \langle \mathbf{v} \rangle = (1/|V|) \int_{V^{\mathrm{f}}} \mathbf{v}\, \mathrm{d}V$ and related to the intrinsic phase average $\mathbf{v}^{\mathrm{f}} = \langle \mathbf{v} \rangle^{\mathrm{f}} = (1/|V^{\mathrm{f}}|) \int_{V^{\mathrm{f}}} \mathbf{v}\, \mathrm{d}V$ by $\mathbf{v}^{\mathrm{D}}(s) = s\phi \mathbf{v}^{\mathrm{f}}(s)$, where $\mathbf{v}$ is the local velocity. Implementation of Equation (1) is difficult, therefore as an alternative approach, modified Darcy's law was suggested by Muskat [17]. Although Equation (1) is adopted by several authors, Darcy's law is rarely adapted as in Reference [17], see also Reference [14]. An effective (instead of absolute $\mathbf{K}$) permeability tensor $\mathbf{K}^{\mathrm{ef}}$ should be used, because the flow is not yet stabilized in the transition region. Also surface tension influence, represented by macrolevel (homogenized) capillary pressure, can be important in the vicinity of the flow front region. In summary, two more functions, relative permeability $k(s)$ and macroscopic capillary pressure $P_{\mathrm{c}}(s)$, both being functions of saturation, must enter into the analysis [17, 18] and modify Darcy's law into

$$\mathbf{v}^{\mathrm{D}}(s) = -\frac{k(s)}{\mu} \mathbf{K} \cdot \nabla (P(s) + P_{\mathrm{c}}(s)) \tag{2}$$

where μ is the resin viscosity, effective permeability $\mathbf{K}^{\mathrm{ef}}(s) = k(s)\mathbf{K}$ (for anisotropic cases it is more accurate to use $K_{ij}^{\mathrm{ef}} = k_{ij}(s) K_{ij}$ (no sum), $k_{ij} \in [0, 1]$, $k_{ij}(0) = 0$ and $k_{ij}(1) = 1$) and $P(s)$ is the intrinsic phase average of the local hydrodynamic pressure $P = \langle p \rangle^{\mathrm{f}} = p^{\mathrm{f}}$ with the property $P(s) = s\, p^{\mathrm{f}}(s)$. Homogenized capillary pressure $P_{\mathrm{c}}(s)$ is a macroscopic analogue of the microscopic pressure p_{c}, it obeys $P_{\mathrm{c}}(1) = 0$ and unlike p_{c}, it acts in the full transition region without being dependent on the actual 'front curvature'. Although the negative sign of the homogenized capillary pressure $P_{\mathrm{c}}(s)$ is usually omitted, we use it with the correct sign to be consistent with the microlevel value. It can be defined as $P_{\mathrm{c}} = 2\gamma \langle H \rangle$, where H is the mean curvature and γ is the resin surface tension. In order to apply gradient in Equation (2), also functional dependence of saturation on spatial variable $\mathbf{x}$ must be known. Equations (1) and (2) reduce to the steady-state formulation in the fully saturated region, i.e. for $s = 1$.

$P_{\mathrm{c}}(s)$ and $k(s)$ must enter macroscopic analysis as known data; therefore they must be determined elsewhere, experimentally or by exploiting homogenization techniques applied to the resin progression results from micro and/or mesolevel. The work of Han [19] with experimental values adopted from other research fields for $P_{\mathrm{c}}(s)$ and $k(s)$ can be named among the earlier attempts to implement Equation (2) in the RTM process. Our objective is to develop a model, and incorporate it into a simulation, that will predict with sufficient accuracy resin progression at the micro and mesolevel and consequently will allow development of methodologies for determination of relative permeability and macroscopic capillary pressure by homogenization techniques. Additional benefits from such formulation are that one can determine the requirements on resin properties and process conditions for favourable filling without the danger of void formation. One can also detect possible filling anomaly that originates at the microlevel and cannot be represented at the macrolevel filling simulation with macroscopic variables.

The numerical modelling of the governing equations for the free boundary at the micro and mesolevel was incorporated as a set of subroutines in a commercial software ANSYS and will be called as free boundary program (FBP). The predictions from FBP have been published for microlevel filling along with methodologies for relative permeability and homogenized capillary pressure determination under some limitations in Reference [20]. Currently, FBP can handle two-dimensional mesolevel filling, its efficiency of calculation was improved by inclusion of several stabilization techniques, improving not only the speed of calculation but also the accuracy of the solution. The aim of this paper is thus description of FBP methodology,

discussion of its numerical aspects and presentation of strategies and techniques for modelling of low capillary number flows.

Not much work has been done in the modelling of free boundary viscous flows at the microlevel and especially at the mesolevel of the RTM manufacturing process. Considering the importance of multi-scale modelling in composites manufacturing, it is crucial to understand and include the influence of micro and mesolevel scales in the process moulding. Many free boundary flows simulations, available nowadays in other fields of research, are applicable to inviscid fluids. Hele–Shaw approximation of thin cavity viscous flows, which is adopted in injection moulding simulations, is not appropriate for RTM micro or mesolevel applications. Three-dimensional simulations of free boundary viscous flows as developed in Reference [21] are exploiting finite differences (and not FE) and are therefore not applicable to mesolevel flows and capillary action influence. Multi-scale simulations as described in References [22, 23] are suited for macrolevel filling and also do not account for the surface tension contribution. Popular method of smoothed particle hydrodynamics is difficult to apply in our case because of the crucial role of the boundary conditions and the viscosity value importance. Tracking of the free boundary by VOF (volume of fluid method [24]) has not been also applied to RTM mesolevel analysis yet. To our knowledge only simulations by the Lattice Boltzman method [25] can handle transient mesolevel filling but require a very different approach. However, due to the numerical stability of the Lattice Boltzman method, no homogenized capillary pressure was included in fibre tows, but instead the surface tension influence at the same level as in inter-tow spaces was used. In comparison, FBP can deal with any level of capillary pressure inside fibre bundles.

Many authors claim that fluid flow analysis in RTM manufacturing process should be coupled with thermal analysis and cure kinetics effects, because resin viscosity is a strong function of temperature and degree of cure, however, no results of real processes are available to support this fact. Obviously, resin properties and process characteristics can be set for the numerical simulation in a way to make this influence significant. On the other hand, actual control of the injection process during manufacturing maintains the mould temperature at a constant value, in order to keep the resin viscosity constant and preferentially at its lowest value. For real resins, especially developed for RTM injection as RTM6 or PR500, the strongest resin viscosity dependence can be modelled as a function of time, which can be achieved in numerical simulations by allowing for variable viscosity without coupling flow and thermal analysis. We present therefore our studies under isothermal conditions, although, in our approach thermal effects inclusion does not introduce any complications.

3. MICROLEVEL ANALYSIS

Resins especially developed for RTM processes usually belong to the group of incompressible Newtonian liquids, corresponding flow in RTM applications has low Reynolds number, gravity can be omitted and by adopting the common restriction to quasi steady-state process, one must solve Stoke's problem [26] in the currently filled domain Ω_{t_k} at each discretized time t_k:

$$\nabla \cdot \mathbf{v} = 0 \quad \text{and} \quad \nabla p = \mu \Delta \mathbf{v} \text{ in } \Omega_{t_k} \tag{3}$$

where $\mathbf{v}$ and p are local velocity vector and pressure, μ is the resin viscosity and $\Delta = \nabla \cdot \nabla$. When fibres are rigid, impermeable and stationary during injection, the following boundary

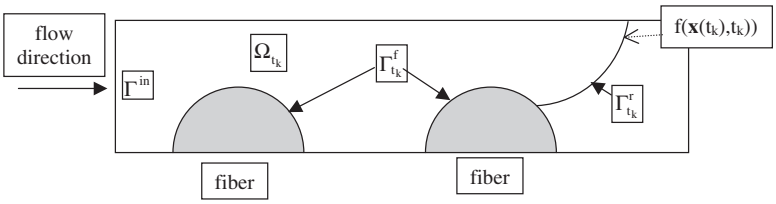

Figure 4. Schematic of flow domain with designations related to Equations (3)–(5).

conditions, under a usual omission of air pressure, must be fulfilled (Figure 4):

$$\textit{At the resin front}: \quad \sigma_{\mathrm{t}}^{\mathrm{v}} = 0 \quad \text{and} \quad \sigma_{\mathrm{n}}^{\mathrm{v}} - p \approx -p = -p_{\mathrm{c}} = -2\gamma H \quad \text{at } \Gamma_{t_k}^{\mathrm{r}} \tag{4a}$$

$$\textit{At the fibre boundary}: \quad \mathbf{v} = \mathbf{0} \quad \text{at } \Gamma_{t_k}^{\mathrm{f}} \tag{4b}$$

$$\textit{At the inlet}: \quad \mathbf{v} = \mathbf{v}_0 \text{ or } p = p_0 \text{ at } \Gamma^{\mathrm{in}} \tag{4c}$$

where $\boldsymbol{\sigma}^{\mathrm{v}}$ is viscous stress tensor, $\mathbf{n}$ stands for the outer unit normal vector to the free front, $\sigma_{\mathrm{n}}^{\mathrm{v}}$ and $\sigma_{\mathrm{t}}^{\mathrm{v}}$ are intrinsic normal and tangential components of the viscous stress vector at the boundary $\Gamma_{t_k}^{\mathrm{r}}$, p_{c} is local capillary pressure given by Young–Laplace equation [27] included in Equation (4a), H is the mean curvature and γ is the resin surface tension. The inlet velocity, $\mathbf{v}_0$, and the inlet pressure, p_0, represent imposed boundary conditions. Besides Equation (4), contact angle must be formed at the resin front-fibre contact point ($\Gamma_{t_k}^{\mathrm{r}} \cap \Gamma_{t_k}^{\mathrm{f}}$). Other boundary conditions such as symmetry or periodicity are related to the particular problem under consideration (Figure 4). Additional condition to move the resin front yields from free surface equation, stating that normal velocity at the free surface is equal to the velocity of this surface outer normal, which in our case reduces to the boundary condition to be imposed on $\Gamma_{t_k}^{\mathrm{r}}$, known as free boundary kinematic condition [26, 28, Chapter 13]

$$\frac{\mathrm{D}f}{\mathrm{D}t} = \frac{\partial f}{\partial t} + \mathbf{v} \cdot \nabla f = 0 \quad \text{at } \Gamma_{t_k}^{\mathrm{r}}, \tag{5}$$

where $f(\mathbf{x}(t), t) = 0$ is an implicit function, where graph describes the moving front $\Gamma_{t_k}^{\mathrm{r}}$, and $\mathbf{x}$ is spatial variable. Initial position of Γ_0^{r} can be assumed identical with Γ^{in} for $\mathbf{v} = \mathbf{v}_0$ or parallel with Γ^{in} in small distance for $p = p_0$. Either the former or the latter assumption does not influence the final flow fronts pattern.

FBP is concerned with the moving flow front, which requires results extraction for a current time t_k, determination of the new resin front position $\Gamma_{t_{k+1}}^{\mathrm{r}}$ at t_{k+1}, stabilization of this new front, application and stabilization of boundary conditions at $\Gamma_{t_{k+1}}^{\mathrm{r}}$ according to Equation (4a), application of other boundary conditions stated in Equations (4b) and (4c) and adjustment of the contact angle, if required. The numerically discretized version of the governing equation of the free surface and the proposed methodology is implemented as subroutines, written by FORTRAN, Maple and APDL (Ansys Parametric Design Language), in ANSYS. Then *the base analysis*, in this case Stoke's problem, is solved by ANSYS CFD FLOTRAN module. This procedure is repeated at each time step. FBP has to deal with the usual problems of moving mesh algorithms with re-meshing of the currently filled domain at each time step, like boundary identification, preventing normal crossing, free boundary looping, etc.

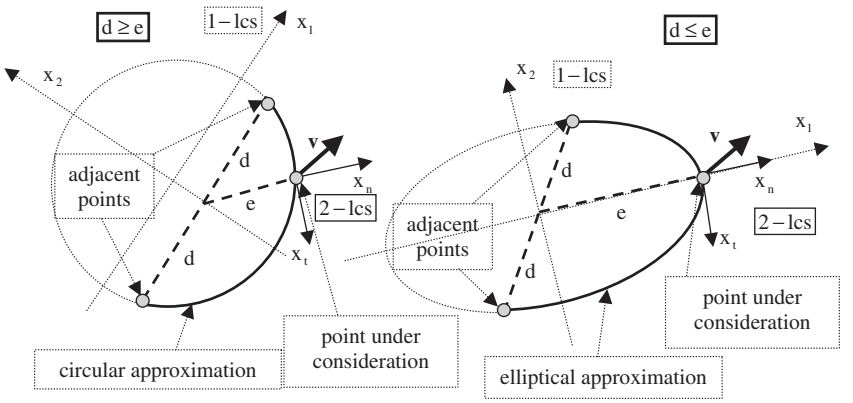

Figure 5. Flow front approximation and local co-ordinate systems definitions.

To describe the details in two-dimensions, one must first, at each frontal point at a current time, $\mathbf{x}_{t_k}^i = \lfloor x_{1,t_k}^i, x_{2,t_k}^i \rfloor$, extract local velocities and create a local co-ordinate system (called 1-lcs as shown in Figure 5), where the flow front is locally approximated by a smooth circular or elliptical curve, which includes two adjacent points, $\mathbf{x}_{t_k}^{i-1}$ and $\mathbf{x}_{t_k}^{i+1}$. Whether circular or elliptical approximation is used, depends on the lengths $d = \|\mathbf{x}_{t_k}^{i+1} - \mathbf{x}_{t_k}^{i-1}\|/2$ and $e = \|\mathbf{x}_{t_k}^i - (\mathbf{x}_{t_k}^{i+1} + \mathbf{x}_{t_k}^{i-1})/2\|$, which are introduced and explained in Figure 5. This permits one to define uniquely the outer normal vector to the flow front. Next, a second local co-ordinate system is created (2-lcs) with the origin at the point under consideration $\mathbf{x}_{t_k}^i$ and axes aligned to the tangential, x_t, and the outer normal vector, x_n, with respect to the approximating curve. The flow front is described locally at the time t_k by $f(\mathbf{x}(t), t) = x_n - g(x_t, t) = 0$ with respect to the 2-lcs, which modifies Equation (5), expressed at the point under consideration, i.e. for $x_{t,t_k}^i = 0$ and $x_{\mathrm{n},t_k}^i = 0$, into

$$\left(\frac{\mathrm{D}f}{\mathrm{D}t}\right)\Bigg|_{(x_{t,t_k}^i=0,\ x_{\mathrm{n},t_k}^i=0,\ t=t_k)} = \left(\frac{\partial g}{\partial t} + v_{\mathrm{n}} - v_t \frac{\partial g}{\partial x_t}\right)\Bigg|_{(x_{t,t_k}^i=0,\ x_{\mathrm{n},t_k}^i=0,\ t=t_k)} = \left(\frac{\partial g}{\partial t} + v_{\mathrm{n}}\right)\Bigg|_{(x_{t,t_k}^i=0,\ x_{\mathrm{n},t_k}^i=0,\ t=t_k)} = 0 \tag{6}$$

since

$$\left(\frac{\partial g}{\partial x_t}\right)\Bigg|_{(x_{t,t_k}^i=0, x_{\mathrm{n},t_k}^i=0,\ t=t_k)} = 0$$

Then the new position of the point under consideration is determined as

$$x_{\mathrm{n},t_{k+1}}^i = x_{\mathrm{n},t_k}^i + \Delta x_{\mathrm{n},t_k}^{i,\alpha} = \Delta t_k v_{\mathrm{n},t_{k+\alpha}}^i = (t_{k+1} - t_k) v_{\mathrm{n},t_{k+\alpha}}^i \tag{7a}$$

and

$$x_{t,t_{k+1}}^i = x_{t,t_k}^i = 0 \tag{7b}$$

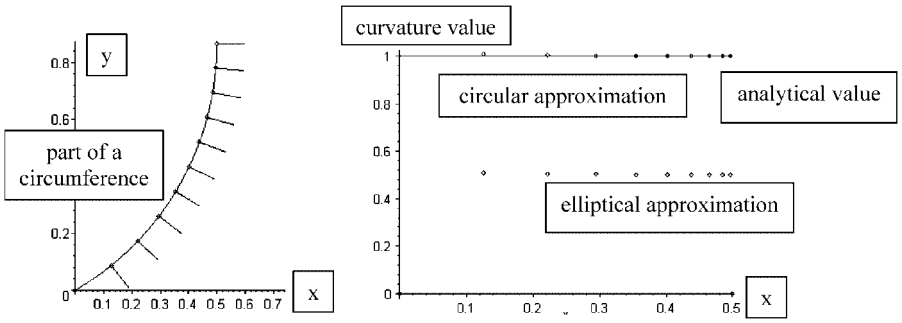

Figure 6. Front shape and outer normals (on the left) and curvature values (on the right) obtained analytically (continues line for curvature value) and from the two distinct approximations for part of a circumference.

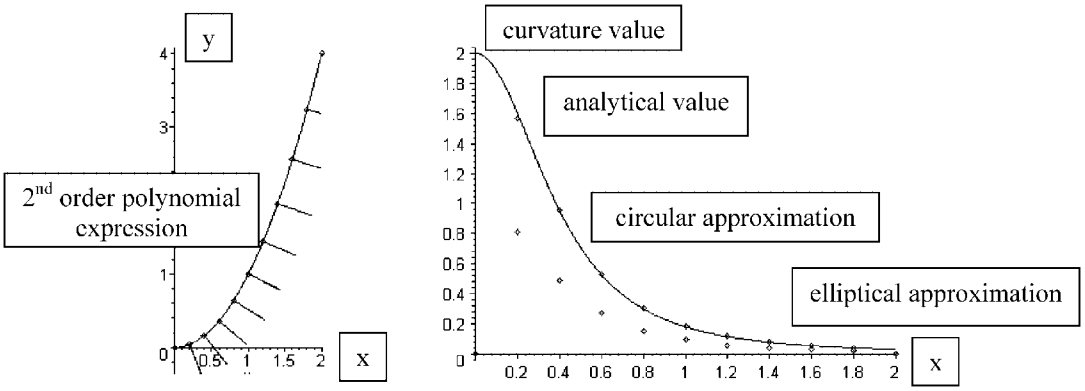

Figure 7. Front shape and outer normals (on the left) and curvature values (on the right) obtained analytically (continues line for curvature value) and from the two distinct approximations for second-order polynomial expression.

where the meaning of the symbol $\alpha \in [0,1]$ will be explained later on. The smooth curve approximation as described above is repeated, now for the new front $\Gamma^{\mathrm{r}}_{t_{k+1}}$, and the surface curvature is determined locally at each point in order to calculate the capillary pressure, which is then imposed as a piece-wise linear function at each frontal line. Finally, other boundary conditions are applied and the base analysis is solved by ANSYS CFD FLOTRAN in the updated domain $\Omega_{t_{k+1}}$.

When $d \geqslant e$, the circular approximation according to Figure 5 is strongly preferable to other types of approximations, as it is justified in Figures 6 and 7. In these figures a comparison of front shape, outer normal and curvature value is presented, when solved analytically and when obtained by the approximations described above. In each frontal point the condition $d \geqslant e$ is fulfilled, however, both kinds, circular as well as elliptical approximations, are used for the sake of comparison. As analytical functions, part of circumference $y = \frac{\sqrt{3}}{2} - \sqrt{1 - (x + \frac{1}{2})^2}$,

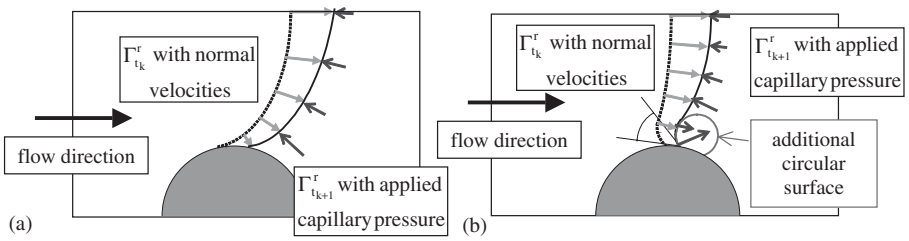

Figure 8. Front progression along fibre surface: (a) without and (b) with the influence of the contact angle θ formation.

$x \in [0, 0.5]$ (Figure 6) and second-order polynomial expression $y = x^2$, $x \in [0, 2]$ (Figure 7) were chosen. It is seen that there are almost no differences in front shapes and outer normals between the analytical values and the two distinct approximations, while, curvature values are strongly influenced by the kind of approximation, which is implemented. It might be added that the case $d \leqslant e$ is not very common during front progression and therefore the elliptical approximation serves here well.

In FBP, there is no need for special treatment of the singularity point at the contact location between the resin and the fibre surface ($\Gamma^r_{t_k} \cap \Gamma^f_{t_k}$). In the case of neglected contact angle formation, resin progression along the fibre surface is ensured by the neighbouring point motion from $\Gamma^r_{t_k}$ (Figure 8(a)). If contact angle is formed, in FBP additional circular surface is created (Figure 8(b)) in order to adjust exactly to the given angle. This radius as well as the contact angle are accurately measurable characteristics, depending on the properties of the three phases: resin–fibre–air, and must enter the analysis as known parameters. Correct position of the additional circle is determined by software Maple module.

As shown in Reference [20], free boundary progression pattern in the same geometry and for the same given contact angle is only dependent on capillary number N_c, defined as $v\mu/\gamma$, where v is a characteristic velocity component of the current case study; and there is no dimensional factor, i.e. only the relative dimension of fibres and their arrangement matters. In fact, real fibre size should be reflected in the radius of the additional circular surface for the contact angle adjustment, however, in real RTM problems this additional surface is never so large to influence the bulk flow front. When capillary number is low, the resin front approaches the constant curvature surface directed by the contact angle and generally low capillary number creates more favourable conditions for injection in view of air entrapment. It was concluded in Reference [20], that surface tension influence at the microlevel cannot be neglected. If it was omitted, all progressions would have the same pattern as for $N_c = \infty$.

A negative effect of low capillary number in view of numerical simulation is that the resin front is more sensitive to the time step magnitude and unphysical non-smoothness are more probable to occur. The resin front $\Gamma^r_{t_k}$ can start to oscillate due to these factors, as it is shown in Figure 9. If the time step is doubled (Figure 9(b)) with respect to the one used in Figure 9(a), local curvature of the new front $\Gamma^r_{t_{k+1}}$ can be at some point unrealistically reversed, creating high capillary pressure in the opposite direction, which will push the front more than necessary against the flow direction. This will create in the next step higher capillary pressure acting in the flow direction, pulling the front more than necessary in the flow direction and this process will lead to oscillations and instability. This phenomenon can stabilize and not

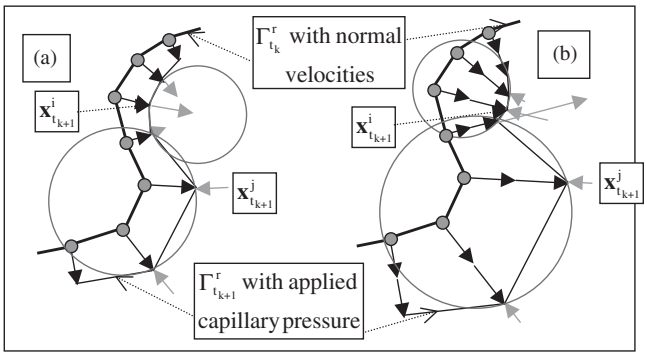

Figure 9. Acceptable front progression (a) and onset of front oscillation due to an extra large time step (b) shown on a part of the free front. Approximating circles used for the local curvature estimation are in red and are shown for points $\mathbf{x}^i_{t_{k+1}}$ and $\mathbf{x}^j_{t_{k+1}}$.

affect the global results, but actually such resin progression will need more time steps than a smooth front movement. For better control, a maximum normal advance (user input) is used to calculate the actual time step Δt_k. Appropriate time step depends on many factors, therefore the best method is to check the flow pattern for oscillations and when it is detected, modify parameters and restart the analysis from the last smooth front. This can be implemented in the FBP in an automated way without user input or judgment.

Two stabilization techniques are implemented in FBP in order to decrease the possibility of front oscillations, which can originate due to unphysical non-smoothness, as a result of LMC violation. The first one is based on 'parameter' α, introduced in Equation (7a) as $\Delta x^{i,\alpha}_{\mathrm{n},t_k} = \Delta t_k v^i_{\mathrm{n},t_{k+\alpha}} = (t_{k+1} - t_k) v^i_{\mathrm{n},t_{k+\alpha}}$. In a fully explicit approach $\alpha = 0$, however, more correctly it might be assumed that

$$v^i_{\mathrm{n},t_{k+\alpha}} = (v^i_{\mathrm{n},t_k} + v^i_{\mathrm{n},t_{k+1}})/2 = (v^i_{\mathrm{n},t_k} + \beta^i_{t_k} v^i_{\mathrm{n},t_k})/2 = v^i_{\mathrm{n},t_k}(1 + \beta^i_{t_k})/2 \tag{8}$$

where parameter $\beta^i_{t_k}$ can be calculated from LMC condition in the form

$$R^i_{t_k} v^i_{\mathrm{n},t_k} = (R^i_{t_k} + \Delta x^i_{\mathrm{n},t_k}) v^i_{\mathrm{n},t_{k+1}} = \beta^i_{t_k}(R^i_{t_k} + \Delta x^i_{\mathrm{n},t_k}) v^i_{\mathrm{n},t_k} \tag{9}$$

where $R^i_{t_k}$ is curvature radius of the free front at $\mathbf{x}^i_{t_k}$. This procedure maintains better LMC especially in significantly curved regions, as it can be seen in Figure 10. An iterative algorithm according to Equations (8) and (9) is included in FBP, where in the first iteration radius $R^i_{t_k}$ from smooth curve approximation is implemented, while in consequent iterations areas formed by straight lines are used to update $\beta^i_{t_k}$. The number of consequent iterations can be equal to zero in the case of fully explicit approach, when $\beta^i_{t_k} = 1 \ \forall i, k$.

The other stabilization algorithm of unphysical non-smoothness is explained in Figure 11. When a 'sharp' angle on the flow front is detected at $\mathbf{x}^i_{t_{k+1}}$, $\mathbf{x}^i_{t_{k+1}}$ is moved to the location in the middle of the normal line, to the original front $\Gamma^{\mathrm{r}}_{t_k}$, connecting its intersection with a straight line between two neighbouring new points $\mathbf{x}^{i-1}_{t_{k+1}}$ and $\mathbf{x}^{i+1}_{t_{k+1}}$ and the sharp location. Also, this algorithm is introduced in an iterative way. It does not include additional LMC verification, therefore it should not be used as principal, but only as a complementary stabilization technique. Concept of the 'sharpness' is stated by the user, i.e. a maximum allowable

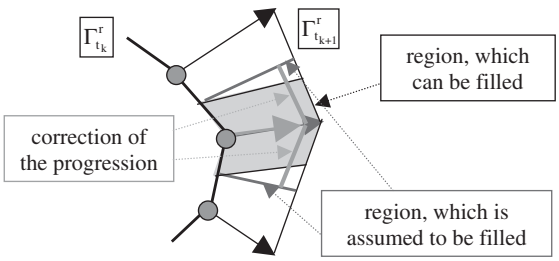

Figure 10. Stabilization technique of LMC in significantly curved fronts.

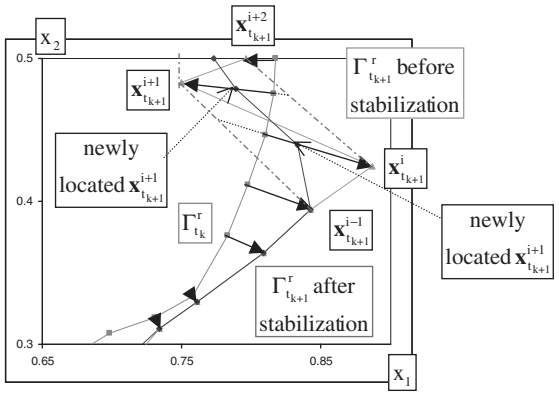

Figure 11. Stabilization technique of unphysical non-smoothness shown on a part of a resin front progression in the global co-ordinate system (x_1, x_2).

angle between the consequent frontal lines is introduced as an input parameter according to the analysis under consideration.

Better LMC can obviously be obtained for finer FE mesh, although, application of this is not very straightforward. Reducing the element size and the time step Δt_k (determined by the maximum front advance $\max_i \Delta x^i_{\mathrm{n},t_{k+1}}$) in a proportional manner does not improve the stability of the flow front. Therefore different control is used for different purposes. Key points are distributed evenly along the flow front and are used for the new front localization and curvature determination. They cannot be very close to each other, as such positions would increase the potential of unphysical non-smoothness. In this approach, generated frontal lines can contain several FE nodes, with more nodes being used along key locations touching some part of the boundary and the time step is reduced independently on the element size or distances between key points.

As already pointed out, FBP is concerned only with the moving flow front, therefore ANSYS capabilities can be fully explored in each base analysis, including gravity, non-Newtonian resin behaviour, coupling with heat transfer analysis and/or fibres deformation and dislocation due to the resin passage. Adaptive h-method or other techniques for improvement of accuracy with less computational time can also be implemented automatically.

4. MESOLEVEL ANALYSIS

In mesolevel analysis liquid flowing along two different levels have to be combined together at each discretized time t_k, which implies that Stoke's problem in inter-tow spaces $\Omega_{t_k}^{S_r}$ and Darcy's problem in intra-tow regions $\Omega_{t_k}^{B_r}$ have to be solved. In fact, Darcy's law must be modified to Brinkman's equation, in order to account for viscous stress at the interface between these two regions, $\Gamma_{t_k}^{S_r-B_r} = \Omega_{t_k}^{S_r} \cap \Omega_{t_k}^{B_r}$, whose importance rapidly decreases with the distance from $\Gamma_{t_k}^{S_r-B_r}$; $\Gamma_{t_k}^{S_r}$ and $\Gamma_{t_k}^{B_r}$ stand for the parts of the free boundary contained in the Stoke's and Brinkman's region, Figure 12. In summary, the governing equations that must be satisfied are

$$\textit{In inter-tow spaces}: \quad \nabla \cdot \mathbf{v} = 0 \quad \text{and} \quad \nabla p = \mu \Delta \mathbf{v} \text{ in } \Omega_{t_k}^{S_r}, \quad \text{(Stoke's problem)} \tag{10a}$$

$$\textit{In intra-tow spaces}: \quad \nabla \cdot \langle \mathbf{v} \rangle = 0 \quad \text{and} \quad \nabla \langle p \rangle^{f} = \mu \Delta \langle \mathbf{v} \rangle - \mu \mathbf{K}^{-1} \cdot \langle \mathbf{v} \rangle \quad \text{in } \Omega_{t_k}^{B_r} \quad \text{(Brinkman's problem)} \tag{10b}$$

FLOTRAN can account for porous media influence by the introduction of distributed resistance. Averaged values in Equation (10) are therefore important mainly from the theoretical point of view, while numerically both, velocity and pressure, maintain their meanings as nodal variables in both regions, preserving all necessary continuity requirements at $\Gamma_{t_k}^{S_r-B_r}$.

It can be concluded from microlevel analysis in Reference [20], that in regular arrangements forming single porous media with uniform pore size, the transition region can be replaced by a sharp flow front (allowing again adopting of quasi steady-state assumption), where capillary pressure has a constant homogenized value and should be applied independently of the actual free front curvature. Values defined in Reference [29] can be used with this purpose, as

$$P_{c,L} = \frac{4\gamma \cos\theta(1-\phi_t)}{\phi_t d_f} \quad \text{and} \quad P_{c,T} = \frac{2\gamma \cos\theta(1-\phi_t)}{\phi_t d_f} \tag{11}$$

for flows along ($P_{c,L}$) and across ($P_{c,T}$) fibre tows, respectively, where d_f is the single fibre diameter and ϕ_t is intra-tow porosity.

4.1. Numerical issues

When both domains $\Omega_{t_k}^{S_r}$ and $\Omega_{t_k}^{B_r}$ are included in the numerical simulation, one has to be careful with the interpretation of the free boundary condition (Equation (5) at microlevel)

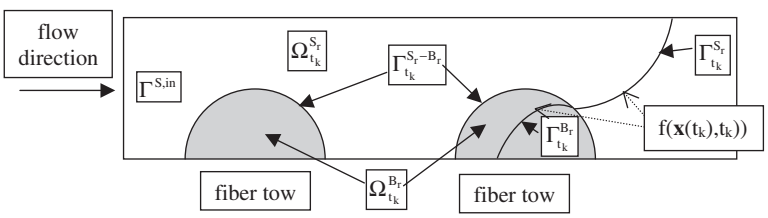

Figure 12. Schematic of flow domain with designations related to Equations (10), (12) and (13).

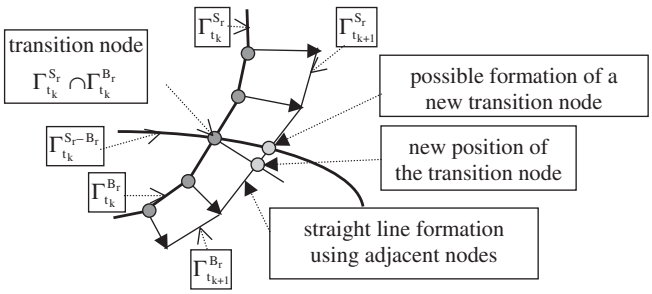

Figure 13. Treatment of the free boundary advance at the transition node.

and capillary pressure application (Equation (4a) at microlevel). Free boundary condition will have two different formulations as follows

$$\frac{\partial f}{\partial t} + \mathbf{v} \cdot \nabla f = 0 \quad \text{at } \Gamma^{S_r}_{t_k} \tag{12a}$$

$$\frac{\partial f}{\partial t} + \frac{1}{\phi_t} \langle \mathbf{v} \rangle \cdot \nabla f = 0 \quad \text{at } \Gamma^{B_r}_{t_k} \tag{12b}$$

Consequently, velocities extracted in intra-tow spaces for the new front determination $\Gamma^{B_r}_{t_{k+1}}$ must be corrected by a factor $1/\phi_t$.

Regarding the capillary pressure application, it holds

$$\sigma^{v}_{n} - p \approx - p = - p_c = - 2\gamma H \quad \text{at } \Gamma^{S_r}_{t_k} \tag{13a}$$

$$\langle p \rangle^{f} = P_c = 2\gamma \langle H \rangle \quad \text{at } \Gamma^{B_r}_{t_k} \tag{13b}$$

From the other boundary conditions only Equation (4c) should be taken into account and it is unchanged, when applied at Stoke's boundary. The same methodology as described in the previous section, including the two stabilization techniques, is used in FBP to track the free front numerically at the mesolevel, only the adjustment of the contact angle is omitted, because it does not apply here.

Now first problems in numerical simulation are clearly visible and are related to the node at the intersection $\Gamma^{S_r}_{t_k} \cap \Gamma^{B_r}_{t_k}$, which we will name as the transition node (Figure 13). The problems are:

- application of Equation (12) is ambiguous at the transition node,
- application of Equation (13) is ambiguous at the transition node.

4.2. Solution

In order to eliminate this ambiguity, FE mesh around the transition node is refined, condition from Equation (13) is not applied, but it is imposed in the way as it should be only at proximal frontal nodes; and automatic correction of the free front to a straight line using two adjacent new nodal positions, as it is shown in Figure 13, is implemented. Such treatment of the transition node implemented in the FBP methodology can ensure correct results of free front boundary pattern and GMC for relatively high capillary numbers.

4.3. *Verification for simple cases*

The first example, verifying the distributed resistance introduction, corresponds to the problem of homogenized (overall) permeability calculation. Flow across in-line arrangement of cylindrical fibre tows with circular cross section of relative radius 0.3 and intra-tow porosity $\phi_t = 0.9$ is considered. Let each tow contain 89 fibres of relative diameter 0.02 with in-line arrangement, yielding intra-tow permeability of 1.28×10^{-4} unit^2. According to homogenization techniques permeability equals to the averaged velocity when a unit macroscopic pressure gradient is imposed on a saturated basic cell containing a unit viscosity liquid, i.e. no FBP methodology is needed in this case. Periodicity of liquid velocity and anti-periodicity of oscillating part of local pressure are applied at external cell boundaries, including simplifications due to symmetry. Results are shown in Figure 14. Velocity and pressure distribution are in agreement with expected and published results [30, 31]. Dimensionless homogenized permeability is determined as 0.0131, which corresponds to the 19% increase against 0.011 of permeability of the same geometry with 'impermeable tow'. It should be remarked in this context, that homogenized permeability cannot depend only on ϕ_t, because dimensional factor is always important. Numerical simulation results are dependent on the 'dimensional' intra-tow permeability. The same value of 1.28×10^{-4} unit^2 could be achieved e.g. for $\phi_t = 0.6$ and 10 fibres of relative diameter 0.12.

In order to verify correctness of the results, LMC error is also calculated and verified as an addition calculation performed by FBP. As the value of the total fluid flux entering and exiting each FE should be zero, the relative LMC error is defined as this total fluid flux divided by the square root of the FE area and by the maximum velocity magnitude associated with this element. In this example, extreme values of LMC error (-0.037 and 0.037) are almost isolated and are located close to the tow surface; but also values of -0.033 and 0.033 can be found along inlet and outlet boundaries. It can thus be concluded that the extreme values of LMC error are of the same order in Stoke's as well as Brinkman's region and therefore introduction of distributed resistance is well suited to model such flows.

Next, verification of numerical simulation results by FBP in intra-tow space with isotropic permeability K between two horizontal plates separated by distance h (i.e. with no-slip condition applied at the tow surface) is presented. This task has an analytical solution for the stabilized steady-state horizontal velocity profile v_x; its variation in vertical direction is

$$\langle v_x \rangle(y) = -\frac{K}{\mu} \frac{d\langle p \rangle^{\mathrm{f}}}{dy} \left(1 - \frac{\cosh((y - h/2)/\sqrt{K})}{\cosh((h/2)/\sqrt{K})} \right) \quad y \in \langle 0, h \rangle \tag{14}$$

It would not be useful to study steady-state flow in fully saturated fibre tow, therefore the analytical velocity profile is compared to the velocity vertical distribution in the stabilized region of free boundary flow infiltration as determined by FBP. For numerical simulation, the following values were chosen based on what is expected in a manufacturing environment: $h = 0.5\,\mathrm{mm}$, constant inlet velocity $\langle v_x \rangle = 1\,\mathrm{mm/s}$; resin viscosity $\mu = 0.05\,\mathrm{Pa\,s}$ (which corresponds e.g. to RTM6), $\phi_t = 0.4$ yielding dimensionless permeability for flow across cylindrical fibres with in-line arrangement of 5.68×10^{-4}. The fibre diameter used was $14.67\,\mu\mathrm{m}$ and distances between their centres were selected to be $16.78\,\mu\mathrm{m}$, which results in a permeability value of $1.6 \times 10^{-7}\,\mathrm{mm}^2$. For the sake of simplicity zero homogenized capillary pressure is used in this verification example. Very fine mesh close to the plate surfaces has to be used, because the velocity profile is practically uniform for these input data and therefore must drop rapidly to

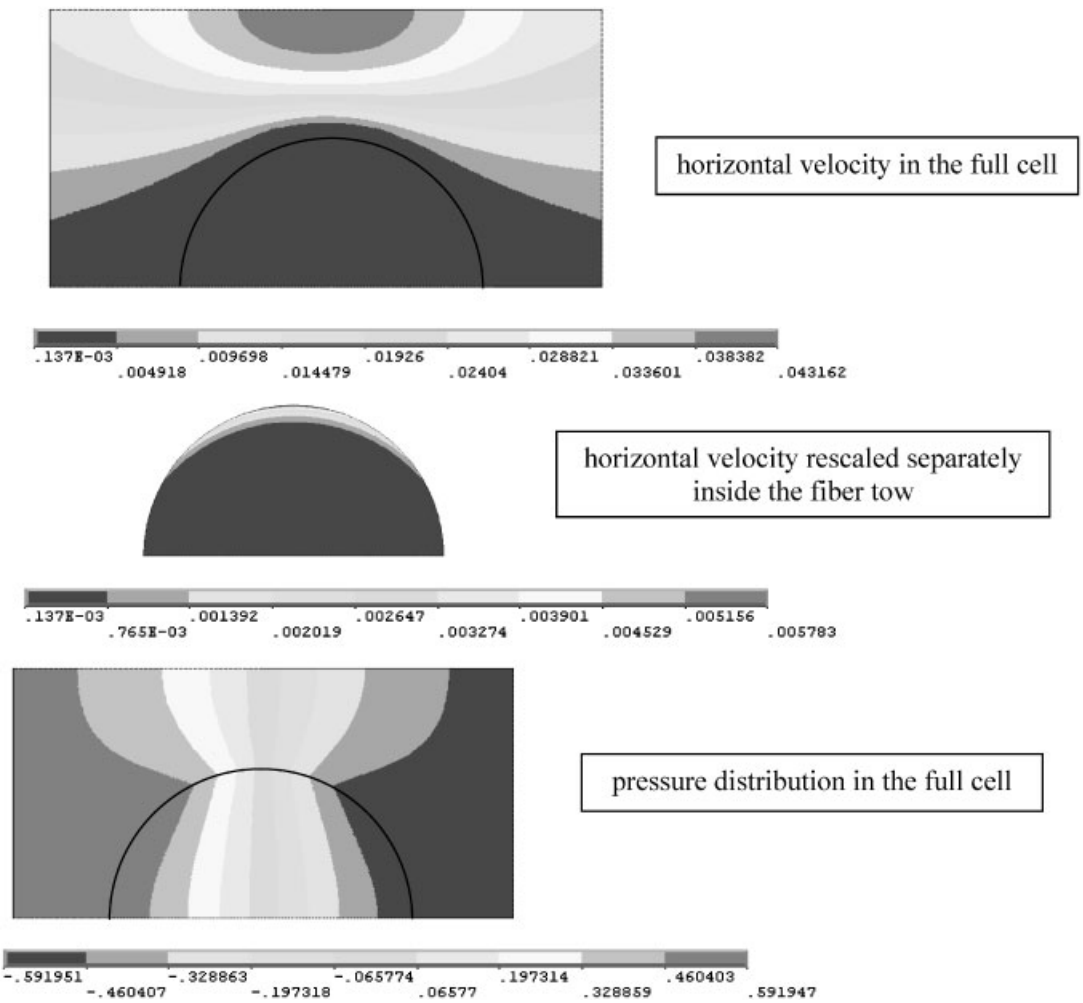

Figure 14. Dimensionless velocity and pressure distribution in the saturated basic cell related to calculation of the homogenized permeability.

zero in this region. The same velocity profile is predicted by the analytical result in Equation (14). Unfortunately, the velocity distribution has strongly non-uniform shape for high value of permeability, for instance $1.6 \times 10^{-2}\,\mathrm{mm}^2$, which is unrealistic for flow across fibres in such a thin cavity. Even though this study is of academic interest, it is used for the analytical value verification. It was verified that in both cases the velocity profile exactly fits the analytical solution, the error in LMC is acceptable and the total resin injected area (two-dimensional simulation) is in very good agreement with the analytical value, i.e. GMC is well-preserved. Free boundary advancement in both simulations is shown in Figure 15. This verification example also allows one to study the influence of the no-slip condition at the wall boundaries on the free front shape at the macrolevel (which cannot be achieved by standard simulation

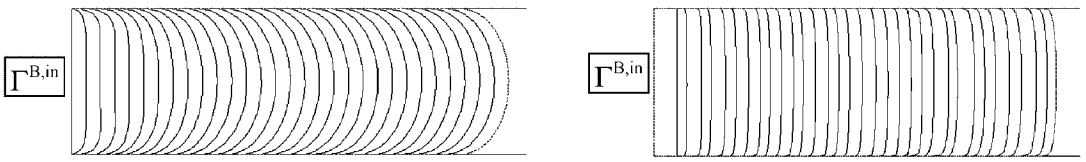

Figure 15. Free boundary advancement in validation example (left: the academic case, right: the real case).

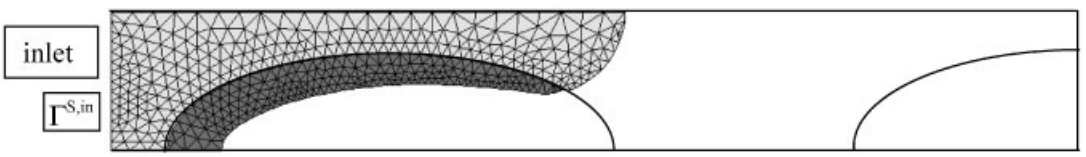

Figure 16. FE mesh for the problem of the total outlet flux adjustment, different colours correspond to filled regions in inter-tow space (blue) and in intra-tow space (violet).

codes), i.e. the appropriateness of the plug flow assumption [32], when no race tracking occurs. Our conclusion might be slightly different from that presented in Reference [32], but this is not the aim of this paper.

4.4. Strategies low capillary number flows

In the case of very low capillary numbers FBP methodology as described in the previous text is not sufficient to preserve an acceptable numerical solution. Especially GMC can be violated, which can be verified in FBP at each discretized time by calculation of the total fluid flux at the outlet, i.e. at the free boundary. Alternative strategies are therefore suggested, explained and verified in the following example.

Let us show the following example: cylindrical fibre tows in in-line arrangement have elliptical cross section with principal semi-axes 0.8 and 0.35 mm and distances between centres 2 and 1 mm in horizontal and vertical direction, respectively. Resin is injected at the left-hand side of the specimen with constant uniformly distributed velocity $v_0 = 1\,\text{mm/s}$ along the height $h = 0.5$ mm. Resin properties are: viscosity $\mu = 0.05$ Pa s and surface tension $\gamma = 0.02$ N/m, yielding the capillary number as 0.0025. Intra-tow porosity is 0.4, giving the total porosity of 0.736. Same dimensions of fibres are used as in the previous verification example implying $K = 1.6 \times 10^{-7}\,\text{mm}^2$. According to Reference [29], for a contact angle of 60°, P_c can be estimated as 2 kPa.

At first, dependence of the total outlet flux on the 'ambiguous' value of the pressure at the transition node was studied. It was verified that this dependence is linear, permitting in two iterative steps to calculate the value to be applied, and in the third step to obtain the correct value of the total outlet flux. At a particular time of the problem, the currently filled region with FE mesh is shown in Figure 16. With no capillary pressure introduced at the transition node, the outlet flux is $-0.67\,\text{mm}^2/\text{s}$ instead of $+0.5\,\text{mm}^2/\text{s}$ and the calculated pressure at the transition node is -53.6 Pa. With capillary pressure $+2.7$ kPa (calculated by the iterations described above) imposed at the transition node, the exact outlet flux of $+0.5\,\text{mm}^2/\text{s}$ is

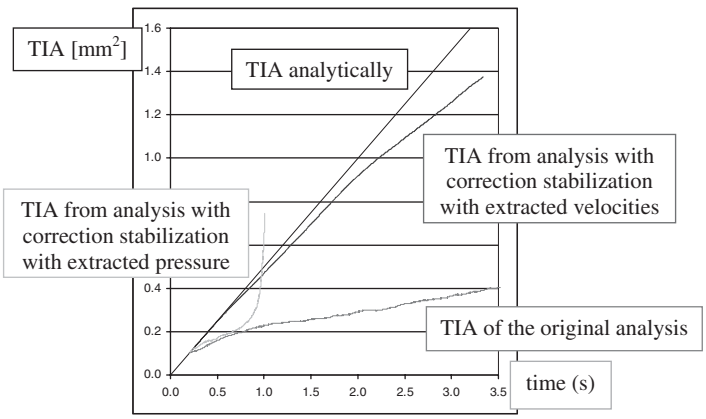

Figure 17. TIA of the analysis with correction stabilization with extracted velocities, with correction stabilization with extracted pressure, and TIA of the original analysis compared with the analytical value.

obtained. Unfortunately, such an approach only distorts local velocities around and especially at the transition node, without the capability to further reduce the LMC error, which is for low capillary numbers concentrated along the free boundary in Stoke's region. Therefore other techniques must be used in order to decrease this error along $\Gamma_{t_k}^{S_r}$.

The two following approaches are suggested:

- When analogy with incompressible elasticity could be used for Stoke's flow, no LMC error concentration around the free front was detected. There is no such simple analogy for mesolevel analysis, but at least velocities or pressures at the interface $\Gamma_{t_k}^{S_r - B_r}$ can be extracted from the original FLOTRAN analysis and additional analysis could be performed, to recalculate velocity distribution in $\Omega_{t_k}^{S_r}$ at each time step. It was verified that such corrections can be significant and we can call this approach as *correction stabilization.*
- The other approach is based on the fact that to eliminate LMC along the free boundary in Stoke's region, capillary pressure to be applied on $\Gamma_{t_k}^{S_r}$ cannot vary much from one key position to another, but should be stabilized before being applied. Since it was concluded at microlevel, that for low capillary number free front $\Gamma_{t_k}^{r}$ approaches constant curvature shape, least square approximation of the capillary pressure by constant or linear function would be desirable. This procedure can be named as *smooth stabilization.*

In order to compare the effectiveness of these two stabilizations, GMC verification in the previous problem was performed, i.e. the total injected resin area (TIA) from infiltrations with correction stabilization and smooth stabilization was compared to TIA from the original analysis (i.e. analysis with neither correction nor smooth stabilization implemented, but with stabilizations from the previous section incorporated) and to TIA analytical value, which is in this case $v_0 h t = 0.5t$. In Figure 17 TIA of the analysis with correction stabilization with extracted velocities at $\Gamma_{t_k}^{S_r - B_r}$, with correction stabilization with extracted pressure at $\Gamma_{t_k}^{S_r - B_r}$, and TIA of the original analysis is compared to the analytical value. It is seen that TIA

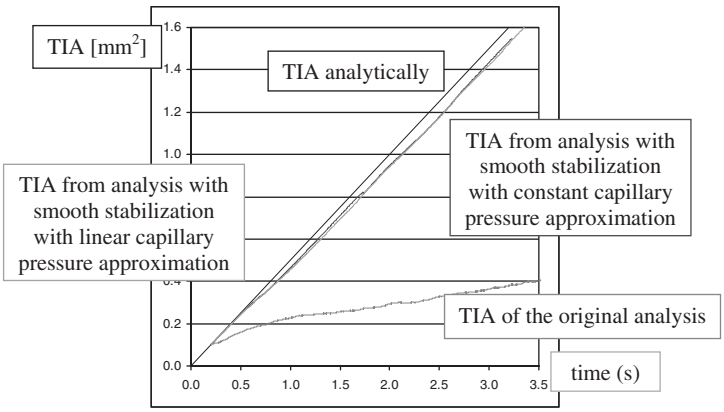

Figure 18. TIA of the analysis with smooth stabilization with linear capillary pressure approximation, with smooth stabilization with constant capillary pressure approximation, and TIA of the original analysis compared with the analytical value.

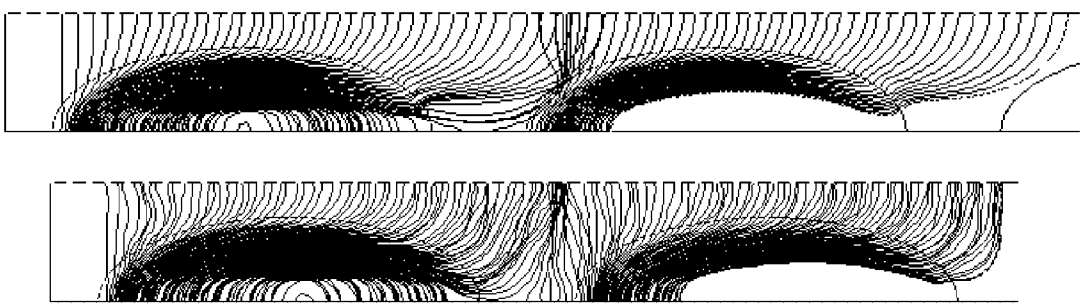

Figure 19. Part of free flow fronts pattern from the analysis with smooth stabilization with constant capillary pressure approximation (above) and correction stabilization with velocities extraction (below).

of the correction stabilization with extracted velocities at $\Gamma_{t_k}^{S_r - B_r}$ acceptably approaches the analytical values. However, correction stabilization has a disadvantage as other FLOTRAN capabilities related to non-Newtonian liquids, coupling with thermal analysis and inclusion of fibre deformation and dislocation would be lost.

Better results were obtained with smooth stabilization implemented, for both linear and constant approximation of the capillary pressure in Stoke's region. In Figure 18 there is a noticeable drop in TIA in early time steps, but this error maintains its magnitude and does not increase along filling time as in the correction stabilization. Free boundary pattern is compared in Figure 19 for correction stabilization with velocity extraction and smooth stabilization with constant capillary pressure approximation. Not much difference can be found between these two patterns, because in these two cases GMC was well-preserved, nevertheless, free fronts from the smooth stabilization are more evenly spaced and are smoother.

5. CONCLUSION

In this article, free boundary progression pattern at micro and mesolevel filling of RTM manufacturing process determined by FBP was discussed. FBP is a free boundary program that integrates routines and interconnecting moduli written in Ansys Parametric Design Language (APDL), FORTRAN and Maple, applied directly to FLOTRAN CFD ANSYS module. Stabilization techniques described in this article were mainly introduced because of the LMC error concentrated along the free boundary of the Stoke's region and are mainly necessary for low capillary number sensitive infiltrations. No problems were detected at the interface between the saturated tow surface and filled inter-tow space.

It should be stressed that FBP belongs to the group of moving mesh algorithms, because free front curvature has been found to be essential to incorporate surface tension effects. FBP has the possibility of restarting the analysis from a specified time step and of modifying parameters related to the analysis for each time step. Implemented stabilization techniques are directed by user specified values and calculation of several characteristics averages to be used in homogenization procedures is also included. FBP has full capability of capturing voids formation and of prediction process and material parameters for favorable filling without risk of dry spots formation. An important step for further development of FBP would be to extend it to three-dimensional problems.

ACKNOWLEDGEMENTS

The firstly named author would like to thank the Portuguese institution for founding the research Fundação para a Ciência e a Tecnologia for the scholarship allowing the development of this work.

REFERENCES

1. Advani SG, Bruschke MV, Parnas RS. Resin transfer molding. In *Flow and Rheology in Polymeric Composites Manufacturing*, Advani SG (ed.). Elsevier: Amsterdam, 1994; 465–516.
2. Advani SG, Dimitrovová Z. Role of capillary driven flow in composite manufacturing. In *Surface and Interfacial Tension*; *Measurement*, *Theory and Application*, Hartland S (ed.). Surfactant Science Series, vol. 119. Marcel Dekker, Inc: New York, 2004; 263–312.
3. Parnas RS, Phelan FR. The effect of heterogeneous porous media on mold filling in resin transfer molding. *SAMPE Quarterly* 1991; **22**:53–60.
4. Parnas RS, Salem AJ, Sadiq TAK, Wang HP, Advani SG. The interaction between micro- and macroscopic flow in RTM preforms. *Composite Structures* 1994; **27**:93–107.
5. Patel N, Lee LJ. Effects of fibre mat architecture on void formation and removal in liquid composite molding. *Polymer Composites* 1995; **16**:386–399.
6. Patel N, Rohatgi V, Lee LJ. Micro scale flow behavior and void formation mechanism during impregnation through a unidirectional stitched fibreglass mat. *Polymer Engineering and Science* 1995; **35**:837–851.
7. Sadiq TAK, Advani SG, Parnas RS. Experimental investigation of transverse flow through aligned cylinders. *International Journal of Multiphase Flow* 1995; **21**:755–774.
8. Binetruy C, Hilaire B, Pabiot J. The interactions between flows occurring inside and outside fabric tows during RTM. *Composites Science and Technology* 1997; **57**:587–596.
9. Binetruy C, Hilaire B, Pabiot J. The influence of fibre wetting in resin transfer molding: scale effects. *Polymer Composites* 2000; **24**:548–557.
10. Sanchez-Palencia E. Non-homogeneous media and vibration theory. *Lecture Notes in Physics*, vol. 127. Springer: Berlin, 1980; 129–157.
11. Ene HI, Polisevski D. *Thermal Flow in Porous Media*. D. Reidel Publishing Company: Dordrecht, 1987.
12. Bruschke MV, Advani SG. A finite element/control volume approach to mold filling in anisotropic porous media. *Polymer Composites* 1990; **11**:291–304.
13. Bruschke MV, Advani SG. A numerical approach to model non-isothermal, viscous flow with free surfaces through fibrous media. *International Journal for Numerical Methods in Fluids* 1994; **19**:575–603.

14. Dave R. A unified approach to modeling resin flow during composite processing. *Journal of Composite Materials* 1990; **24**:22–41.
15. Lin M, Hahn HT, Huh H. A finite element simulation of resin transfer molding based on partial nodal saturation and implicit time integration. *Composites A* 1998; **29A**:189–198.
16. Shojaei A, Ghaffarian SR, Karimian SMH. Numerical simulation of three-dimensional mold filling process in resin transfer molding using quasi-steady state and partial saturation formulations. *Composites Science and Technology* 2002; **62**:861–879.
17. Muskat M. *The Flow of Homogeneous Fluids through Porous Media*. McGraw-Hill: New York, 1937.
18. Collins RE. *Flow of Fluids through Porous Media*. Reinhold Publishing Corporation: New York, 1961.
19. Han K. Analysis of dry spot formation and changes in liquid composite molding. *Ph.D. Thesis*, The Ohio State University, 1994.
20. Dimitrovová Z, Advani SG. Analysis and characterization of relative permeability and capillary pressure for free surface flow of a viscous fluid across an array of aligned cylindrical fibres. *Journal of Colloid and Interface Science* 2002; **245**:325–337.
21. Tome MF, Filho AC, Cuminato JA, Mangiavacchi N, McKee S. GENSMAC3D: a numerical method for solving unsteady three-dimensional free surface flows. *International Journal for Numerical Methods in Fluids* 2001; **37**:747–796.
22. Chang W, Kikuchi N. Analysis of composite molding using the homogenization method. *International Journal of Computational Fluid Dynamics* 1996; **7**:49–77.
23. Simacek P, Advani SG. A numerical model to predict fibre tow saturation during liquid composite molding. *Composites Science and Technology* 2003; **63**:1725–1736.
24. Hirt CW, Nichols BD. Volume of fluid (VOF) method for the dynamics of free boundaries. *Journal of Computational Physics* 1981; **39**:201–225.
25. Spaid MAA, Phelan FR. Modeling void formation dynamics in fibrous porous media with the Lattice Boltzman method. *Composites A* 1998; **29A**:749–755.
26. White FM. *Fluid Mechanics*. McGraw-Hill: New York, 1994.
27. Adamson AW. *Physical Chemistry of Surfaces*. Wiley: New York, 1982.
28. Whitham GB. *Linear and Nonlinear Waves*. Wiley: New York, 1974.
29. Ahn KJ, Seferis JC, Berg JC. Simultaneous measurements of permeability and capillary pressure of thermosetting matrices in woven fabric reinforcements. *Polymer Composites* 1991; **12**:146–152.
30. Ranganathan S, Phelan FR, Advani SG. A generalized model for the transverse fluid permeability in unidirectional fibrous media. *Polymer Composites* 1996; **17**:222–230.
31. Papathanasiou TD. A structure oriented micromechanical model for viscous flow through square arrays of fibre clusters. *Composites Science and Technology* 1996; **56**:1055–1069.
32. Gibson AG. Modification of Darcys law to model mould interface effects in composites processing. *Composites Manufacturing* 1992; **3**:113–118.

